ARTICLE OPEN

Check for updates

POM121 O-GlcNAcylation facilitates bone metastasis in non-small cell lung cancer through enhanced c-MYC nuclear import and ECM reprogramming

Yi-Zhe Ren[1,3], Ming-Na Zhao[1,3], Feng-Lin Du[2], Lei Wu[1], Lin Wang[1]✉ and Jia-Tao Lou[1]✉

Bone metastasis is a devastating complication of non-small cell lung cancer (NSCLC), critically impairing patient survival. Nevertheless, the underlying molecular mechanisms driving this aggressive process remain incompletely elucidated. To systematically investigate these mechanisms, we compared a highly bone-metastatic NSCLC subpopulation with its parental cells. Notably, we identified elevated expression of O-linked β-N-acetylglucosamine transferase (OGT) in the metastatic subpopulation. We further demonstrated that O-GlcNAcylation at the Ser199 site of the nuclear pore protein POM121 is markedly increased and drives NSCLC bone metastasis. Mechanistically, O-GlcNAcylation of POM121 attenuates its interaction with the E3 ubiquitin ligase TRIM21, thus antagonizing ubiquitination and stabilizing POM121. Accumulated POM121 enhances the nuclear import of the oncogenic transcription factor c-MYC. Nuclear c-MYC subsequently orchestrates transcriptional activation of downstream extracellular matrix (ECM)-related genes. Collectively, we elucidate a previously unrecognized OGT-POM121-c-MYC-ECM axis that critically drives NSCLC bone metastasis. Crucially, clinical analysis reveals that high levels of OGT, POM121, and c-MYC positively correlate with adverse clinical outcomes. These findings establish the OGT-POM121-c-MYC-ECM axis as a potential diagnostic biomarker and a promising therapeutic target for NSCLC bone metastasis.

Oncogene; https://doi.org/10.1038/s41388-026-03687-y

INTRODUCTION

Non-small cell lung cancer (NSCLC) ranks among malignancies with the highest mortality rates due to metastatic dissemination and limited therapeutic options [1]. Over 70% of patients present with locoregional or distant metastasis at diagnosis [2], with bone being a predominant site that severely compromises quality of life [3]. Notably, 30–40% of NSCLC patients develop bone metastases, correlating with a median survival of only 6 months [4, 5]. Current therapies (bisphosphonates, denosumab) target osteoclast-mediated bone destruction but lack tumor-specific precision [6–8]. Thus, defining molecular drivers of bone metastasis is imperative for developing targeted interventions.

Post-translational modifications (PTMs), including glycosylation, phosphorylation, acetylation, methylation, and palmitoylation, orchestrate cancer hallmarks by modulating protein stability, localization, activity and interactions [9]. Among these PTMs, O-GlcNAcylation has emerged as a critical PTM, wherein dysregulation of its homeostatic balance is implicated in tumor initiation and progression. This nutrient-sensitive PTM dynamically conjugates O-linked N-acetylglucosamine to serine/threonine residues of nuclear, cytoplasmic, and mitochondrial proteins [10, 11]. Its dynamic cycling is exclusively regulated by a binary enzyme system: O-GlcNAc transferase (OGT) for installation and O-GlcNAcase (OGA) for removal [12]. O-GlcNAcylation modulates signaling cascades, protein trafficking and stability, transcriptional programs, epigenetic regulation, mitochondrial dynamics, and cellular survival pathways [13]. Accumulating evidence underscores the critical regulatory roles of O-GlcNAcylation in driving metastasis in cancers. For example, FOXA1 O-GlcNAcylation promotes breast cancer metastasis by stabilizing FOXA1 and orchestrating transcription of metastasis regulators [14]. Glucose metabolism in macrophages induces O-GlcNAcylation of lysosomal Cathepsin B at S210, elevating mature Cathepsin B secretion to promote metastasis and chemoresistance [15]. However, systematic assessment of O-GlcNAcylation in NSCLC bone metastasis and functional dissection of its target protein mechanisms remain unexplored.

Nuclear pore complexes (NPCs) form selective channels through the nuclear envelope to mediate nucleocytoplasmic trafficking. As essential molecular conduits, NPCs comprise approximately 30 distinct nucleoporins (Nups) assembled in multiple copies [16, 17]. POM121, a core transmembrane Nup, maintains cellular homeostasis through structural and functional integrity [18]. Structurally, POM121 contains an N-terminal transmembrane domain and an extramembranous region harboring two putative bipartite nuclear localization signals (NLSs) that engage importin α/β complexes. Positioned at the NPC central channel, POM121 directly binds importin β1 to license nuclear import of transcription factors, thereby implying its potential role in tumorigenesis and progression [19]. A recent study confirmed that H3K18la enhances immune

[1]Department of Laboratory Medicine, Shanghai General Hospital, Shanghai Jiao Tong University School of Medicine, Shanghai, China. [2]School of Life Sciences, Bengbu Medical University, Bengbu, China. [3]These authors contributed equally: Yi-Zhe Ren, Ming-Na Zhao. ✉email: wanglin987654321@126.com; loujiatao@sjtu.edu.cn

Received: 2 September 2025 Revised: 11 December 2025 Accepted: 25 January 2026
Published online: 02 February 2026

escape of NSCLC by binding to the POM121 promoter regions and upregulating POM121 expression [20]. However, whether POM121 undergoes O-GlcNAcylation modifications and contributes to NSCLC bone metastasis remains unexplored.

In this study, employing antibody-conjugated beads and sWGA-beads followed by LC-MS/MS, we identified robust O-GlcNAcylation of the nucleoporin POM121 in highly metastatic bone NSCLC subpopulations. Moreover, we experimentally demonstrate that O-GlcNAcylation attenuates POM121's interaction with the E3 ubiquitin ligase TRIM21, thereby stabilizing POM121 protein levels. Critically, O-GlcNAcylated POM121 facilitates nuclear translocation of the oncogenic transcription factor c-MYC, which subsequently activates an extracellular matrix (ECM) remodeling program to drive bone metastasis. These findings reveal an O-GlcNAcylation-dependent regulatory axis governing NSCLC bone metastasis, positioning targeted inhibition of POM121 O-GlcNAcylation as a promising therapeutic strategy for clinical translation.

MATERIALS AND METHODS

Cell culture and transfection

Non-small cell lung carcinoma (NSCLC) cell lines NCI-H460, NCI-H1299, NCI-H1437, and HEK293T cells were obtained from American Type Culture Collection (ATCC). Bone-metastatic NSCLC sublines were generated as previously described [21]. Parental NSCLC cells and their bone-metastatic derivatives were cultured in RPMI 1640 medium (Gibco, cat#C11875500CP) supplemented with 10% fetal bovine serum (FBS; Gibco, cat#A5669701) and 1% penicillin-streptomycin (Gibco, cat#15140163). HEK293T cells were maintained in DMEM (Gibco, cat#C11995500CP) with 10% FBS and 1% penicillin-streptomycin. NSCLC cells were infected with indicated viruses and subjected to antibiotic selection for enrichment and single clone selection before the assays. Transient transfections were performed using Lipofectamine 2000 (Invitrogen, cat#11668019) according to the manufacturer's protocol.

Recombinant plasmid construction

To generate recombinant plasmids encoding POM121, the full-length POM121 cDNA was cloned into the pCMV-Myc (tag) epitope-tagging vector and pLVX-Hygro lentiviral expression plasmid. Gene-specific primers were designed using SnapGene v5.3.2 (Insightful Science), flanked by appropriate restriction enzyme sites compatible with the target vectors. Total RNA was reverse-transcribed into cDNA using the PrimeScript RT Reagent Kit (Takara Bio, cat#RR047A) according to the manufacturer's protocol. PCR amplification was performed with KOD-Plus-Neo high-fidelity DNA polymerase (ToYoBo, cat#KOD-401) under optimized thermocycling conditions. The resulting PCR products were separated by electrophoresis on a 1% agarose gel, and DNA fragments of expected sizes were excised and purified using the MiniBEST Agarose Gel DNA Extraction Kit (Takara Bio, cat#9762). Purified PCR products and plasmid vectors were digested with restriction endonucleases. Digested fragments were purified again to remove enzyme contaminants. Ligation was performed using DNA ligase or ClonExpress Ultra One Step Cloning Kit (Vazyme, cat#C115), which employs homologous recombination-independent cloning to achieve seamless assembly with high efficiency. The reaction mixture was incubated at 55 °C for 30 min and then transformed into competent *E. coli* DH5α cells via heat shock. Positive clones were selected by antibiotic resistance and validated by colony PCR.

For site-directed mutagenesis of POM121 O-GlcNAcylation sites (Ser113, Ser150, Ser170, Ser199, Thr203, Ser429), alanine substitutions were introduced using the KOD-Plus-Mutagenesis Kit (ToYoBo, cat#SMK-101). Mutagenic primers were designed to replace serine/threonine codons without altering adjacent sequences. All the DNA sequences of the POM121 constructs were assessed by Sanger sequencing.

To knock down POM121 expression, short hairpin RNA (shRNA) sequences targeting POM121 (Table S6) were cloned into the pLKO.1-puro lentiviral vector using AgeI/EcoRI restriction sites, followed by lentiviral packaging and stable cell line generation.

Lentivirus packaging, infection and stable cell lines construction

The lentiviral vectors, including pLVX-Hygro for protein expression and pLKO.1-puro for shRNA-mediated knockdown, were co-transfected with packaging plasmids psPAX2 and envelope plasmid pMD2.G into HEK293T cells at a mass ratio of 4:3:1 (transfer plasmid: psPAX2: pMD2.G) using X-tremeGENE HP DNA Transfection Reagent (Roche, cat#06366236001). Viral supernatant was harvested 36 h and 72 h post-transfection, filtered through 0.45 μm PES membranes to remove cellular debris, and concentrated via ultracentrifugation (27,000 rpm for 2 h at 4 °C; Beckman Coulter SW 32 Ti rotor). Viral pellets were resuspended in 100 μl PBS, aliquoted, and stored at −80 °C.

For stable cell line construction, target cells were infected with lentiviral particles at a multiplicity of infection (MOI) of 5–20. Selection antibiotics were applied 48 h post-transduction. For knockdown lines, puromycin (1.5 μg/ml, 7 days) was added for pLKO.1-puro-based constructs. For rescue or overexpression lines, Hygromycin B (15 μg/ml, 7 days) was added for pLVX-Hygro-based constructs. To avoid knockdown by shRNA, we made a synonymous mutation.

Animal models and ethical compliance

BALB/c nude mice (aged 6–8 weeks) were housed under specific pathogen-free (SPF) conditions (temperature: 22 ± 1 °C; humidity: 55 ± 5%; 12 h light/dark cycle) with free access to autoclaved food and water. All procedures were approved by the Institutional Animal Care and Research Advisory Committee of the Shanghai Institute of Biochemistry and Cell Biology, Chinese Academy of Sciences (IACUC Approval No. IBCB0063), and conducted in compliance with the Guide for the Care and Use of Laboratory Animals (NIH Publication No. 80-23, revised 1996).

Generating NSCLC Bone-metastatic Sublines

As the schematic diagram illustrating (Fig. S1A), to generate NSCLC orthotopic xenograft tumor model, 1×10^5 GFP and luciferase-expressing NSCLC (H460, H1299, H1437) cells were intratracheally transplanted into BALB/c nude mouse, with tumor growth assessed by bioluminescence imaging. As intracardiac injection of tumor cells recapitulated the steps of metastasis including circulation, bone homing and colonization [22]. 4 weeks later, bone-metastatic tumor cells were subsequently isolated from hind limbs and injected into the mice again. After three rounds of selection, we obtained the stably bone-metastatic subpopulation, referred to as NSCLC-BM sublines (H460-BM, H1299-BM, H1437-BM).

Intracardiac (IC) Injection

BALB/c nude mice were randomly assigned to different groups. Intracardial injections were performed after anesthetized by intraperitoneal injection of sterile avertin (250 mg/kg) as previously described [23]. For intracardial injection, 1×10^5 luciferase-expressing NSCLC cells were injected into the left ventricle of mouse by high-resolution echocardiography-guided percutaneous left ventricular intracavitary injection.

Bioluminescence Imaging (BLI)

Tumor-bearing mice were anesthetized via isoflurane inhalation (induction: 3% in 100% O_2; maintenance: 1.5–2%) using a calibrated vaporizer. D-Luciferin (PerkinElmer, cat#122799) was dissolved in sterile PBS and administered intraperitoneally at 150 mg/kg body weight. After 5 min, bioluminescence images of mice were acquired simultaneously using an IVIS Lumina LT Series III (PerkinElmer). The photon flux (photons s^{-1}) within the interested region delineated by BLI signals was calculated using the Living Image software. Blinding was not performed during analysis because the metastasis of tumor had an obvious characteristic towards BLI.

Transwell invasion assays

The invasive capacity of tumor cells was evaluated using Corning Transwell inserts (24-well plate, 8 μm pore size; cat#3422) coated with Matrigel basement membrane matrix (Corning, cat#356234). Matrigel was diluted 1:8 in ice-cold serum-free RPMI 1640 medium on ice to prevent polymerization, and 60 μL of the solution was uniformly applied to the upper chamber membrane followed by incubation at 37 °C for 4 h to form a gel layer. Cells in logarithmic growth phase (from ATCC) were trypsinized with 0.25% trypsin-EDTA (Gibco, cat#C25200072), centrifuged at 500 × g for 3 min, and resuspended in 5% FBS RPMI 1640 medium. Cell density was adjusted to 25×10^4 cells/mL (validated by > 95% viability via trypan blue exclusion), and 200 μL of the suspension was seeded onto the Matrigel-coated inserts. The lower chambers were filled with 600 μL of chemoattractant (10% FBS; Gibco) in RPMI 1640 medium. After 48 h of incubation at 37 °C under 5% CO_2 (duration optimized through preliminary time-course

assays). Invaded cells attached to the membrane underside were fixed with 4% paraformaldehyde (BBI, cat#E672002-0500) for 30 min at room temperature and stained with 0.2% crystal violet (Solarbio, cat#G1062) for 20 min, non-invaded cells on the upper membrane surface were removed with a cotton swab. Membranes were rinsed in PBS, air-dried, and imaged using a Nikon Eclipse 80i microscope (20× objective). Five randomly selected fields per membrane were analyzed by counting crystal violet-positive cells; quantification was performed using ImageJ software with particle analysis parameters set to >50 pixels^2 area and 0.2–1.0 circularity threshold. Each experiment included triplicate inserts per condition and was repeated three times independently, $n = 3$ independent experiments; mean ± SEM; $^*p < 0.05$, $^{**}p < 0.01$, $^{***}p < 0.001$, unpaired t-test.

Histological and Immunofluorescent (IF) Analyses

For hematoxylin and eosin (H&E) staining, dissected femurs underwent fixation in 4% paraformaldehyde at 4 °C for 24 h to preserve tissue architecture. Bones were decalcified by incubation in 0.5 M EDTA (solution replaced daily) for 2–3 weeks, with endpoint flexibility confirming decalcification completion. Decalcified tissues were dehydrated through a graded ethanol series, cleared in xylene, and embedded in paraffin wax.

For H&E staining, sections were deparaffinized in xylene, rehydrated through graded ethanol, and stained with Mayer's hematoxylin for 8 min followed by eosin Y for 2 min. H&E images were acquired with Nikon Eclipse 80i microscope.

For immunofluorescent (IF) staining, cell samples were fixed in 4% paraformaldehyde solution for 15 min at room temperature, permeabilized with 0.3% Triton X-100 for 10 min, and blocked with 1% BSA for 30 min. Primary antibodies (TABLE S5) were applied overnight at 4 °C, followed by Alexa Fluor-conjugated secondary antibodies (TABLE S5) at 4 °C for 2 h. Nuclei were counterstained with DAPI (1 μg/mL) for 5 min. IF images were acquired using Leica TCS SP8 confocal or Olympus FV3000 confocal microscope, and immunofluorescent densities were quantified using the FV31S-SW Viewer and ImageJ software.

RNA extraction and quantitative real-time PCR (RT-qPCR) analyses

Total RNA was isolated from cells or tissues utilizing TRIzol reagent (Thermo, cat#15596018CN) followed by purification using the RNA Clean & Concentrator Kit (ZYMO Research, cat#R1016), according to the respective manufacturers' protocols. Subsequently, complementary DNA (cDNA) synthesis was performed via reverse transcription using the PrimeScript RT Reagent Kit (TaKaRa, cat#RR047A) as per the manufacturer's instructions. Quantitative real-time PCR (RT-qPCR) analysis was then conducted on an ABI QuantStudio 3 instrument (Applied Biosystems) employing ChamQ Universal SYBR qPCR Master Mix (Vazyme, cat#Q711-03) according to the kit's protocol. Relative gene expression levels were calculated using the $2^{[-\Delta\Delta Ct]}$ method, with β-actin mRNA serving as the endogenous normalization control. The nucleotide sequences of all primers utilized in this study are detailed in (TABLE S6).

Nucleocytoplasmic fractionation

Nucleocytoplasmic fractionation was performed to isolate nuclear and cytoplasmic components using the Nuclear and Cytoplasmic Protein Extraction Kit (Beyotime, cat#P0028) according to the manufacturer's instructions. Cells were resuspended in ice-cold Cytoplasmic Extraction Buffer and lysed on ice. The cytosolic fraction was subsequently harvested by centrifugation at 1000 × g for 5 min at 4 °C. Pelleted nuclei were washed once in Cytoplasmic Extraction Buffer and resuspended in Nuclear Extraction Buffer for lysis at 4 °C for 60 min. The soluble nuclear fraction was then collected by centrifugation at 5000 × g for 5 min at 4 °C. All isolated fractions were aliquoted and stored at −80 °C prior to downstream analysis.

Immunoprecipitation (IP) and Immunoblotting Assays

For IP, NSCLC cells were lysed on ice in lysis buffer (Cell Signaling Technology, cat#9803S) supplemented with protease inhibitor cocktail (Roche, cat# 4693132001), followed by sonication (80% amplitude, 20 s pulses repeated with 60 s intervals) for 6 min on ice. The lysates were centrifuged at 13,000 × g for 10 min at 4 °C to remove insoluble material, and the clarified supernatants were harvested. Protein A/G magnetic beads (Thermo, cat#88802), primary antibody (TABLE S5; validated for IP), species-matched IgG antibody (TABLE S5), or Succinylated Wheat Germ Agglutinin Agarose beads (sWGA-beads, VectorLabs, cat#AL-1023S) were pre-incubated with lysis buffer at room temperature for 4 h under rotation. The clarified lysates were then added to these pre-incubated beads and incubated further at 4 °C for 4 h under rotation. Following the incubation, the beads were collected and washed three times with ice-cold wash buffer (50 mM Tris pH 7.4, 150 mM NaCl, protease inhibitor cocktail) to remove non-specifically bound proteins.

For immunoblotting, whole-cell/tissue lysates or the immunoprecipitated samples bound to beads were resuspended or diluted in SDS loading buffer and subjected to standard SDS-PAGE followed by Western blotting using the primary antibodies detailed in (TABLE S5). The blotting membranes were imaged using a Tanon 5200 Chemiluminescent Imaging System (Tanon) with multiple exposure times, and band intensities were subsequently quantified using ImageJ software.

Cycloheximide (CHX) assay for protein stability

To assess the stability of POM121 protein variants, a cycloheximide (CHX) chase assay was employed to inhibit new protein synthesis. Cells overexpressing either POM121-WT or the S199A mutant, alongside cells transfected with POM121-WT and subsequently treated with either DMSO or the OGT inhibitor (ST-045849, TOCRIS, cat#6775, 20 μM), were treated with cycloheximide (CHX, MCE, cat#HY-12320, 100 μg/mL) combined with MG132 (MCE, cat#HY-13259, 25 nM). Following treatment initiation, cells were harvested at the designated time points (0, 2, 4, 6, or 24 h). POM121 protein levels were then quantified by Western blot analysis, and the relative half-life was calculated from the resulting decay kinetics.

Mass spectrometry analysis of strip-complex and POM121 O-GlcNAcylation sites

Protein complexes enriched via Streptococcus pneumoniae wheat germ agglutinin (sWGA) lectin affinity beads and anti-Myc (tag) immunoprecipitation (IP) beads targeting recombinant O-GlcNAcylated POM121 were excised from SDS-PAGE gels. These strips contained either O-GlcNAc-modified POM121 or its interacting partners. The resulting peptides were analyzed by liquid chromatograph-mass spectroscopy/mass spectroscopy (LC-MS/MS) at Shanghai Applied Protein Technology (Table S2).

Proteomics Analysis of POM121 Interactome

To identify POM121-binding proteins in bone-metastatic NSCLC cells (H460BM line), we performed co-immunoprecipitation (Co-IP) using anti-POM121 antibody or IgG control. Immunoprecipitated pellets were subjected to on-bead tryptic digestion followed by liquid chromatography-tandem mass spectrometry (LC-MS/MS) analysis, as previously described [21]. Peptides were separated via a nano-flow ultra-high-performance liquid chromatography system (Easy-nLC 1200, Thermo) and analyzed on a Q Exactive HF-X mass spectrometer (Thermo) operated in data-dependent acquisition (DDA) mode. Mass spectra were acquired using Xcalibur software (v4.0, Thermo) with profile spectrum data type.

Raw MS data were processed using MaxQuant software (v2.0.3.0). Database searches were conducted against the human Swiss-Prot database [24], allowing up to two missed cleavages and a minimum peptide length of 7 amino acids. The peptide and protein false discovery rates (FDRs) were fixed at a significance level less than 0.01. The data is shown in TABLE S3.

Transcriptome-seq and bioinformatic analyses

Transcriptomes in NSCLC cells were sequenced using the Illumina sequencing technology following standard procedures, with three biological replicates in this assay.

Raw transcriptome sequencing reads were aligned to homo sapiens reference genome GRCh38 using HISAT package to allows multiple alignments to initially remove a portion of the reads based on quality and a maximum of two mismatches [25]. The differentially expressed mRNAs were selected with log2 (fold change) > 1 or log2 (fold change) <-1 and with statistical significance (p-value < 0.05). The data is shown in TABLE S4.

Gene set enrichment analysis (GSEA)

We performed gene set enrichment analysis (GSEA) to identify biologically relevant pathways associated with the experimental conditions. A pre-ranked gene list was generated by sorting all differentially expressed genes based on their fold change values. This list was then analyzed using the GSEA software [26].

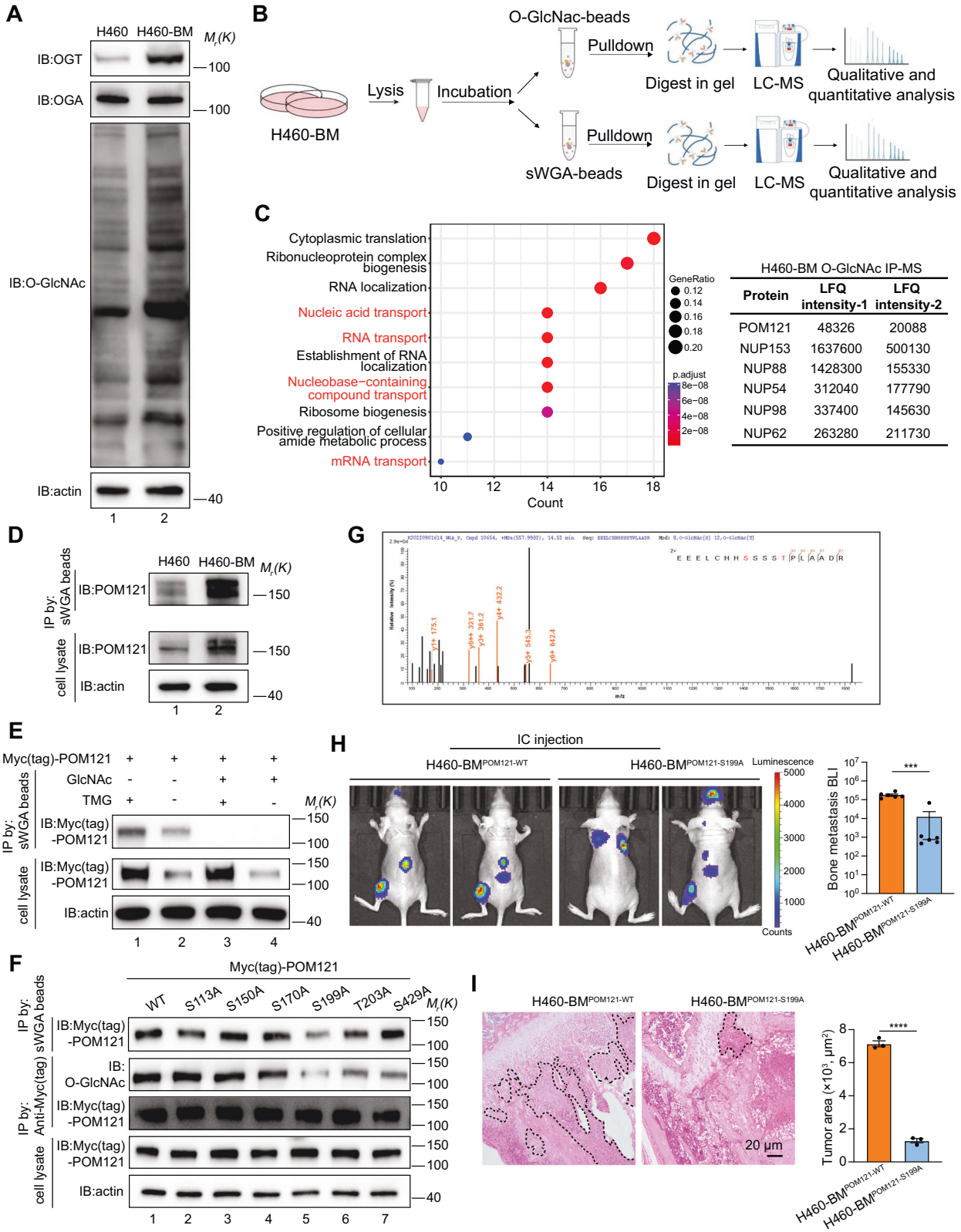

Gene Ontology (GO) enrichment analysis

We conducted Gene Ontology (GO) term enrichment analysis to identify significantly enriched biological processes associated with the target gene set. This analysis was implemented using the R package clusterProfiler (v4.0). To control for false discoveries, we applied the Benjamini-Hochberg (BH) procedure for multiple testing correction, with a false discovery rate (FDR) threshold of 0.05. Enriched GO terms belonging to the biological process (BP) and molecular function (MF) ontology were visualized to highlight functionally relevant pathways.

Fig. 1 O-GlcNAcylation of POM121 at Ser199 promotes bone metastasis in NSCLC. A Protein levels of OGT, OGA and O-GlcNAc in bone-metastatic H460-BM subline and parental H460 cells. Blots are representative of three independent experiments. **B** Schematic of pulldown strategy to identify O-GlcNAc-modified proteins contributing to enhanced bone metastasis in H460-BM cells. **C** Left, significantly enriched ($p < 0.05$) biological processes (GO analysis) for O-GlcNAc-modified proteins in H460-BM cells (top 10 pathways shown). Right, Enrichment of O-GlcNAcylation nucleoporins identified by mass spectrometry. **D** O-GlcNAcylation protein levels of POM121 in bone-metastatic H460-BM subline and parental H460 cells. O-GlcNAcylated proteins were pulled down using sWGA-beads. Blots are representative of three independent experiments. **E** H460-BM cells expressing Myc (tag)-POM121 were treated with or without OGA inhibitor Thiamet G (TMG, 10 mM, 24 h). GlcNAc (+) indicates that sWGA-beads were pre-blocked with GlcNAc (500 mM, 24 h) prior to pulldown. Immunoprecipitation (IP) and immunoblots (IB) were performed using the indicated antibodies. Data are representative of three independent experiments. **F** H460-BM cells expressing Myc (tag)-POM121 and mutations were subjected to sWGA-beads pulldown or anti-Myc (tag)-IP. Immunoblots identified Ser199 as an O-GlcNAc modification site. Data are representative of three independent experiments. **G** Mapping the O-GlcNAcylated residue Ser199 on POM121 by liquid chromatography-tandem mass spectrometry (LC-MS/MS). **H**, **I** O-GlcNAcylation of POM121 at the Ser199 site in NSCLC promotes bone metastasis in nude mouse model. **H** Bioluminescence imaging of nude mice four weeks after intracardiac injection of H460-BM or H460-BM$^{POM121\text{-}S199A}$ cells (1×10^5 cells/mouse). Data are represented as mean ± SEM; $n = 6$ mice/group, ***$p < 0.001$, unpaired t-test. **I** Representative H&E staining and tumor area quantifications of bone metastasis sections from mice in (**H**). Dashed lines demarcate tumor boundaries. Scale bar, 20 μm. Data are represented as mean ± SEM; ****$p < 0.0001$, unpaired t-test.

Statistical analyses

Data are presented as mean ± SEM throughout the manuscript. A minimum sample size of ($n = 3$ for samples or 6 for mice) per group was required to detect the pre-specified effect size with statistical significance. To determine statistically significant differences between experimental groups and their corresponding controls, we performed Student's t-tests. Significant differences, defined as $p < 0.05$, are explicitly indicated on the figures or detailed in the figure legends. Associations between two variables were assessed using Pearson's correlation analysis to derive the correlation coefficient. Unless otherwise specified in the figure legends, all experiments were performed in triplicate.

RESULTS

POM121 exhibits marked O-GlcNAcylation in the bone-metastatic H460-BM subline

In our previous study, we established a bone-metastatic cell model to investigate the mechanisms underlying bone metastasis in NSCLC [23]. Briefly, athymic nude mice were intracardially inoculated with the NSCLC cell line H460; bone-metastatic tumor cells were subsequently isolated from hind limbs. After three rounds of selection, we obtained the stably bone-metastatic subpopulation, referred to as H460-BM (Fig. S1A). This subline exhibited significantly enhanced metastatic potential in Transwell assays versus parental H460 cells (Fig. S1A). Accumulating evidence indicates that the post-translational modification O-GlcNAcylation drives metastasis in various cancers. We therefore sought to determine whether O-GlcNAcylation drives bone metastasis in NSCLC. We examined the O-GlcNAcylation levels in H460 cells and bone-metastatic subline H460-BM. We found that H460-BM cells, exhibited significantly higher global O-GlcNAcylation levels than the parental cell line (Fig. 1A), suggesting that O-GlcNAcylation may promote bone metastasis in NSCLC. Since OGT is the sole and essential enzyme responsible for catalyzing O-GlcNAcylation and OGA is the enzyme that removes O-GlcNAcylation, we assessed the expression levels of OGT and OGA in H460 and H460-BM cells. We found that H460-BM cells expressed higher levels of OGT (Fig. 1A), which elevates the global O-GlcNAcylation level in H460-BM cells. Given elevated OGT expression in H460-BM, we investigated the impact of O-GlcNAcylation on NSCLC bone metastasis by modulating O-GlcNAc levels in parental H460 and H460-BM cells using either the OGA inhibitor Thiamet G (TMG) or OGT-targeting siRNA (si-OGT) (Fig. S1B). Strikingly, TMG treatment of parental H460 cells significantly increased global O-GlcNAcylation and enhanced invasion capacity, whereas OGT knockdown in H460-BM cells effectively reduced protein O-GlcNAcylation and diminished cellular metastatic potential (Fig. S1B).

To identify specific O-GlcNAcylated proteins driving bone metastasis in H460-BM cells, we performed affinity purification using O-GlcNAc antibody-conjugated beads and succinylated wheat germ agglutinin agarose (sWGA) beads incubated with H460-BM lysates, followed by LC-MS/MS analysis (Fig. 1B). This approach identified 563 O-GlcNAc-modified proteins in H460-BM cells (TABLE S1). Interestingly, pathway analysis revealed significant enrichment of these O-GlcNAcylated proteins in nucleocytoplasmic transport pathways, with nuclear pore complex (NPC) proteins significantly enriched (Fig. 1C). Subsequent sWGA-bead immunoprecipitation confirmed O-GlcNAcylation of multiple nucleoporins in H460 bone-metastatic subline (Fig. S1C), implicating Nups O-GlcNAcylation in NSCLC bone metastasis.

Among these nucleoporins, POM121 displayed markedly differential O-GlcNAcylation between H460-BM and parental H460 cells: robust modification in metastatic cells versus minimal levels in parental cells (Fig. 1D). This differential O-GlcNAcylation correlated with OGT upregulation in H460-BM cells (Fig. 1A), prompting us to validate direct OGT-POM121 interaction through co-immunoprecipitation (Fig. S1D). Crucially, the catalytically inactive OGT H568A mutant failed to induce POM121 O-GlcNAcylation, demonstrating that POM121 O-GlcNAcylation is strictly dependent on OGT enzymatic activity (Fig. S1E). Consistently, OGA inhibition elevated POM121 O-GlcNAcylation in H460-BM cells (Fig. 1E), while pre-blocking sWGA-beads with N-Acetyl-D-glucosamine (GlcNAc) abolished POM121 pulldown, confirming O-GlcNAc-specific binding (Fig. 1E). Collectively, these results demonstrate metastasis-specific O-GlcNAcylation of POM121 in H460-BM cells.

O-GlcNAcylation at S199 site of POM121 promotes NSCLC bone metastasis

To validate the functional role of POM121 O-GlcNAcylation in bone metastasis, we performed anti-POM121 immunoprecipitation followed by LC-MS analysis of H460-BM lysates (TABLE S2). This identified six candidate O-GlcNAcylation sites on POM121: S113, S150, S170, S199, T203, and S429 (Fig. S1F). Site-directed mutagenesis demonstrated that the S199A mutation substantially reduced O-GlcNAcylation versus wild-type POM121, establishing S199 as the primary modification site (Fig. 1F), with LC-MS/MS directly confirming O-GlcNAcylation at S199 (Fig. 1G). To assess functional significance, we generated H460-BM cells expressing the POM121^{S199A} mutant (referred to as H460-BM$^{POM121\text{-}S199A}$). Transwell invasion assays demonstrated significantly impaired invasion capacity in mutant cells (Fig. S1G). Consistent with this, H460-BM$^{POM121\text{-}S199A}$ subline exhibited reduced bone metastasis burden in nude mice at three weeks post-intracardiac injection versus parental H460-BM group (Fig. 1H), with histopathology confirming fewer and smaller metastatic lesions (Fig. 1I). Collectively, these results establish site-specific O-GlcNAcylation of POM121 at S199 as a critical driver of H460 cells bone metastasis.

O-GlcNAcylation mediates stabilization of POM121

Protein O-GlcNAcylation dynamically regulates cellular functions by modulating protein stability, subcellular compartmentalization,

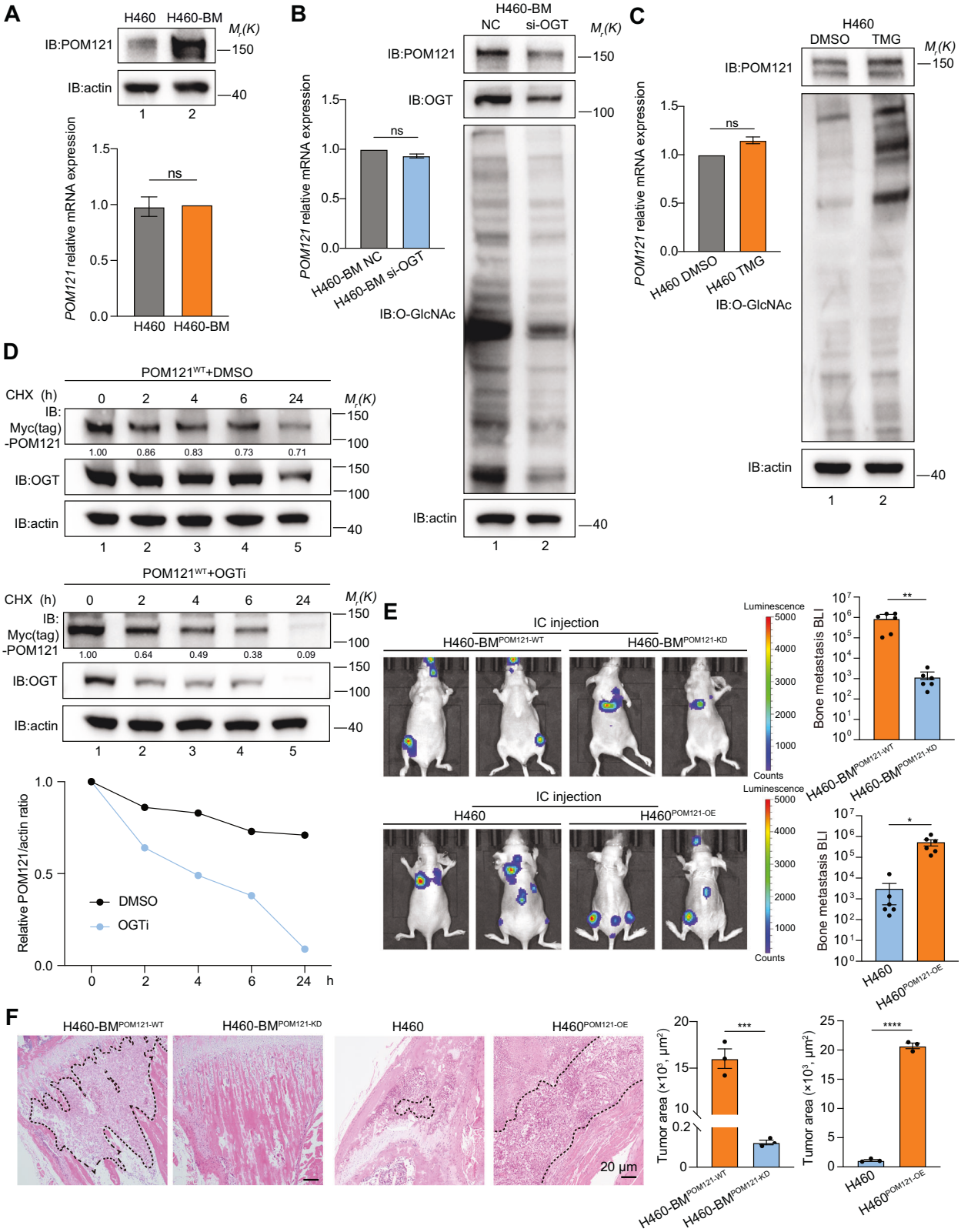

enzymatic activity, and biomolecular interactions [27–29]. To define how POM121 O-GlcNAcylation promotes NSCLC bone metastasis, we first assessed its effects on subcellular localization and protein stability. Immunofluorescence revealed unchanged nuclear membrane localization of POM121 in H460-BM versus parental H460 cells despite differential O-GlcNAcylation (Fig. S2A), but immunoblotting showed markedly elevated POM121 protein in H460-BM with unchanged mRNA levels (Fig. 2A). This uncoupling of protein abundance from transcriptional expression indicates that O-GlcNAcylation enhances POM121 stability at the

Fig. 2 O-GlcNAcylation stabilizes POM121 to promote bone metastasis in NSCLC. A Comparison of POM121 expression in parental H460 and bone-metastatic H460-BM sublines. Top, Immunoblot of POM121 protein levels. Bottom, RT-qPCR analysis of *POM121* mRNA. Data representative of three independent experiments; (ns, not significant, $p > 0.05$, unpaired t-test). **B** Effect of OGT knockdown on POM121 protein stability. H460-BM cells transfected with negative control (NC) or OGT-targeting siRNAs were analyzed by RT-qPCR (left) and immunoblot (right). Data representative of three experiments; (ns, not significant, $p > 0.05$, unpaired t-test). **C** Effect of OGA inhibition on POM121 stability. H460 cells treated with DMSO or TMG (10 mM, 24 h) were analyzed by RT-qPCR (left) and immunoblot (right). Data representative of three experiments; (ns, not significant, $p > 0.05$, unpaired t-test). **D** OGT-dependent O-GlcNAcylation stabilizes POM121. Cycloheximide (CHX, 100 µg/mL) chase assay in cells overexpressing Myc (tag)-POM121 and treated with DMSO or an OGT inhibitor (OGTi, ST-045849, 20 µM, 24 h). Top, Immunoblots of Myc (tag)-POM121. Bottom, Quantification of protein expression. Data representative of three experiments. **E**, **F** Stabilization of POM121 protein in NSCLC promotes metastasis in nude mouse model. **E** Bioluminescence imaging of nude mice four weeks after intracardiac injection. Top, H460-BM and H460-BM$^{POM121\text{-}KD}$ cells (1×10^5 cells/mouse); Bottom, H460 and H460$^{POM121\text{-}OE}$ cells (1×10^5 cells/mouse). Data are represented as mean ± SEM; $n = 6$ mice/group, $^{**}p < 0.01$, $^{*}p < 0.05$, unpaired t-test. **F** Histological validation and tumor area quantifications of bone metastasis. Representative H&E-stained sections from mice in (**E**). Dashed lines demarcate tumor boundaries. Scale bar, 20 µm. Data are represented as mean ± SEM; $^{***}p < 0.001$, $^{****}p < 0.0001$, unpaired t-test.

post-translational level. Consistently, reducing O-GlcNAcylation via si-OGT or OGT inhibitor (OGTi) in H460-BM significantly decreased POM121 protein without altering mRNA (Fig. 2B, S2B) or localization (Fig. S2C). Conversely, OGT overexpression or TMG treatment in H460 cells increased POM121 protein independently of mRNA (Fig. 2C, S2B). Critically, modulating O-GlcNAc levels by altering OGT expression affected POM121^{WT} abundance but not the O-GlcNAc-deficient POM121^{S199A} mutant (Fig. S2D). To definitively confirm the role of O-GlcNAc modification in enhancing POM121 protein stability, we conducted Cycloheximide (CHX)-chase assays to confirm accelerated POM121 degradation upon OGTi-mediated O-GlcNAcylation suppression (Fig. 2D) and inherent instability of POM121^{S199} versus wild-type (Fig. S2E). Collectively, these findings establish that O-GlcNAcylation post-translationally enhances POM121 stability.

To validate that O-GlcNAcylation-mediated POM121 stabilization drives NSCLC bone metastasis, we generated POM121-knockdown H460-BM cells (H460-BM$^{POM121\text{-}KD}$) and POM121-overexpressing H460 cells (H460$^{POM121\text{-}OE}$). H460-BM$^{POM121\text{-}KD}$ exhibited significantly impaired invasion capacity in vitro, while H460$^{POM121\text{-}OE}$ suggested potentially enhanced metastatic capability (Fig. S2F). Importantly, in vivo intracardiac injection in athymic nude mice revealed substantially diminished bone metastasis colonization by H460-BM$^{POM121\text{-}KD}$ versus markedly augmented incidence and burden in H460$^{POM121\text{-}OE}$ (Fig. 2E). Histopathological examination of bone sections revealed that mice injected with H460-BM$^{POM121\text{-}KD}$ cells showed minimal tumor burden, characterized by nearly undetectable metastatic foci and sparse tumor cell infiltration. In stark contrast, H460$^{POM121\text{-}OE}$ cells generated extensive metastatic lesions with dense tumor cell clusters (Fig. 2F). These findings establish O-GlcNAcylation-mediated POM121 stabilization as a key driver of NSCLC bone metastasis.

O-GlcNAcylated POM121 evades ubiquitin-dependent degradation by blocking TRIM21 binding

To delineate how O-GlcNAcylation stabilizes POM121, we characterized its degradation pathways by treating POM121^{S199A} mutant cells (degradation-prone) with ubiquitin-proteasome inhibitor MG132 or autophagy-lysosome inhibitor bafilomycin A1 (BafA1). MG132 significantly increased both protein abundance and ubiquitination of POM121^{S199A} (Fig. 3A), whereas BafA1 showed negligible effects (Fig. 3B), indicating predominant ubiquitin-proteasome-mediated degradation. Crucially, enhancing O-GlcNAcylation via TMG suppressed POM121 ubiquitination while increasing its protein expression and O-GlcNAc modification, but failed to reduce ubiquitination in the O-GlcNAc-deficient POM121^{S199A} mutant (Fig. 3C). These data demonstrate that O-GlcNAcylation antagonizes POM121 ubiquitination to stabilize the protein.

To mechanistically delineate how O-GlcNAcylation antagonizes POM121 ubiquitination, we performed immunoprecipitation-mass spectrometry (IP-MS) identifying the E3 ubiquitin ligase TRIM21 as a top interactor (TABLE S3), with co-IP validating direct POM121-TRIM21 binding (Fig. 3D). Comparative analysis revealed significantly attenuated POM121-TRIM21 interaction in bone-metastatic H460-BM versus parental H460 cells, correlating with diminished ubiquitination and elevated POM121 abundance in metastatic cells (Fig. 3E). Reciprocally, OGT overexpression in H460 cells impaired POM121-TRIM21 binding, while OGT knockdown in H460-BM enhanced the interaction (Fig. 3F). Crucially, TMG treatment or OGT overexpression disrupted POM121^{WT}-TRIM21 interaction but failed to reduce the binding between the O-GlcNAc-deficient POM121^{S199A} mutant and TRIM21 (Fig. 3G). Collectively, these data demonstrate that O-GlcNAcylation at S199 impedes TRIM21 recognition, suppressing ubiquitination and stabilizing POM121.

O-GlcNAcylation impedes TRIM21 recognition to stabilize nucleoporins: a conserved mechanism in NSCLC

To determine if O-GlcNAcylation-dependent blockade of TRIM21 recognition represents a conserved stabilization mechanism in NSCLC, we analyzed additional O-GlcNAcylated Nups in H460-BM cells (Fig. 1C). sWGA pulldown confirmed elevated O-GlcNAcylation and protein abundance of NUP153, NUP88, and NUP54 in metastatic H460-BM cells versus parental cells (Fig. S3A). OGT overexpression enhanced Nups O-GlcNAcylation, attenuated TRIM21 binding, and increased protein levels—recapitulating the POM121 mechanism (Fig. S3B). Modulating OGT expression in both cell lines demonstrated that O-GlcNAcylation impairs Nups-TRIM21 interaction (Fig. S3C). Moreover, O-GlcNAcylation of Nups weakened the Nups-TRIM21 interaction, thereby antagonizing ubiquitination and enhancing Nups protein stability in metastatic H460-BM cells (Fig. S3D). Critically, Kaplan-Meier survival analysis of the NSCLC cohort from GSE37745 database revealed that high expression of POM121, NUP153, NUP88 and NUP54 correlates with poor NSCLC prognosis (Fig. S3E), indicating that O-GlcNAcylation-mediated disruption of TRIM21 binding—which suppresses ubiquitin-dependent nucleoporin degradation—represents a conserved stabilization mechanism contributing to bone metastasis pathogenesis.

POM121 drives bone metastasis via enhanced c-MYC nuclear import

Having established that O-GlcNAcylation-stabilized POM121 drives NSCLC bone metastasis, we investigated how increased POM121 abundance promotes metastasis. As a nuclear pore component facilitating nuclear import, POM121's role was probed through RNA sequencing of H460-BM versus H460-BM$^{POM121\text{-}KD}$ cells (TABLE S4). Transcriptome analysis revealed a POM121-dependent gene signature, with Gene Set Enrichment Analysis (GSEA) showing significant enrichment of c-MYC oncogenic programs in POM121-expressing metastatic cells versus POM121-knockdown controls (Fig. 4A). To validate POM121-

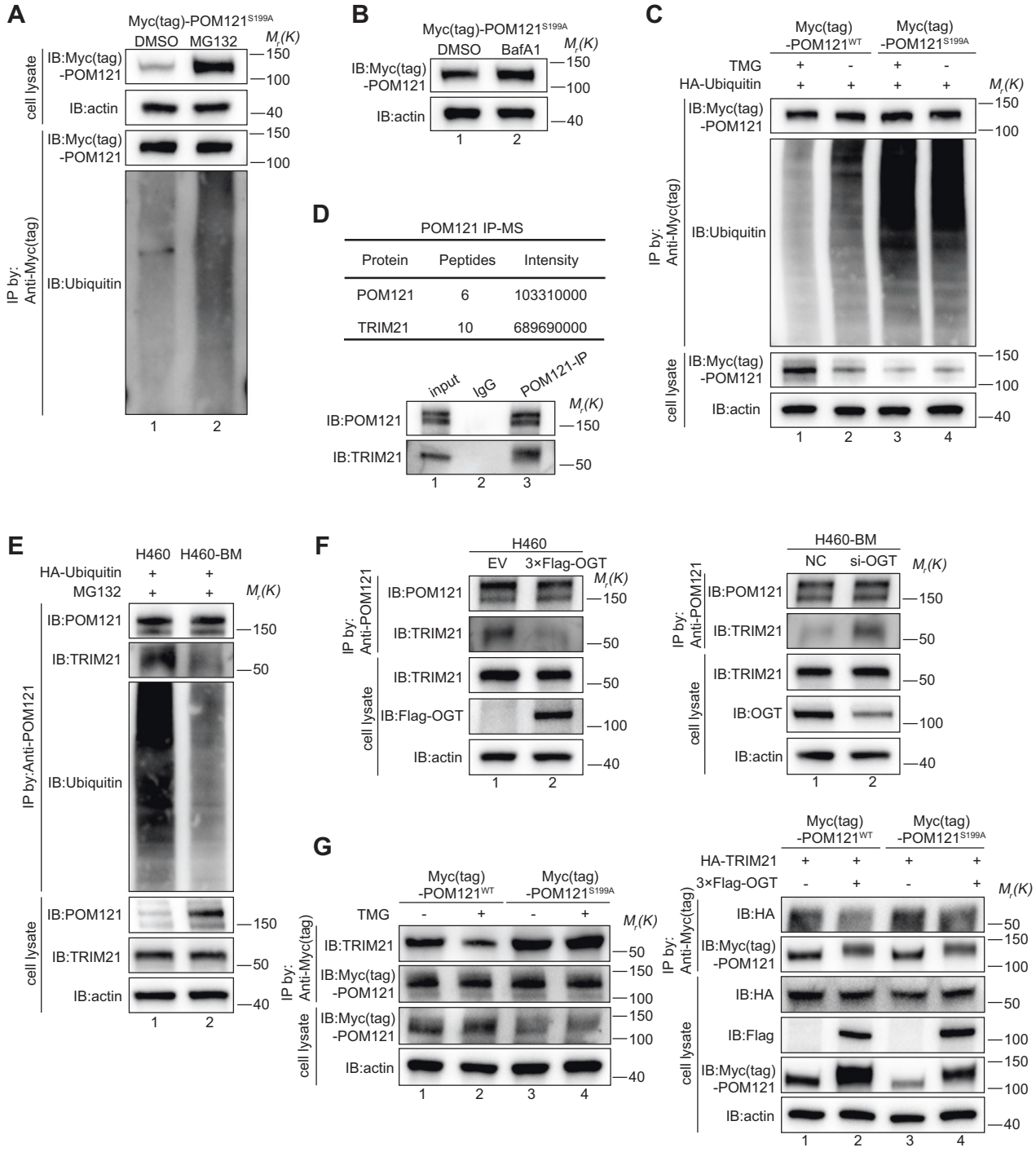

dependent c-MYC nuclear import, nucleocytoplasmic fractionation revealed that POM121 depletion severely impaired c-MYC nuclear accumulation (Fig. 4B), independently confirmed by immunofluorescence showing diminished nuclear import efficiency in POM121-deficient cells (Fig. 4C). Conversely, POM121 overexpression in low-POM121 H460 cells significantly enhanced c-MYC nuclear translocation (Fig. 4D). Critically, this regulatory axis was physiologically relevant: bone-metastatic H460-BM cells exhibited predominant nuclear c-MYC localization compared to parental H460 cells (Fig. 4E). These data establish POM121 as an essential nuclear pore component governing c-MYC nuclear import in NSCLC.

Building on O-GlcNAcylation-mediated POM121 stabilization as a regulator of nucleocytoplasmic trafficking, we employed pharmacological and genetic approaches. Reduction of O-GlcNAcylation via si-OGT or OGTi in H460-BM cells significantly attenuated c-MYC nuclear import (Fig. 4F, S4A, S4B), whereas OGT overexpression or TMG treatment in H460 cells enhanced O-GlcNAcylation and promoted c-MYC nuclear accumulation (Fig. 4F, S4C). Crucially, the O-GlcNAc-deficient POM121^{S199A} mutant exhibited diminished c-MYC nuclear translocation versus wild-type (Fig. 4G), consistent with immunofluorescence results (Fig. S4D). These data demonstrate that O-GlcNAcylation-

Fig. 3 O-GlcNAcylation at Ser199 stabilizes POM121 by antagonizing TRIM21-mediated ubiquitination. A Proteasomal degradation mediates S199A mutant instability. Cells overexpressing Myc (tag)-POM121^{S199A} were treated with DMSO or MG132 (proteasome inhibitor, 25 nM, 24 h). Top, Immunoblot of Myc (tag)-POM121. Bottom, Ubiquitinated proteins immunoprecipitated with anti-Myc (tag) antibody and blotted with anti-Ubiquitin antibody. Data representative of three independent experiments. **B** Lysosomal degradation is dispensable for S199A mutant turnover. Cells overexpressing Myc (tag)-POM121^{S199A} were treated with DMSO or BafA1 (bafilomycin A1, lysosome inhibitor, 100 nM, 24 h). Immunoblot of Myc (tag)-POM121. Data representative of three experiments. **C** O-GlcNAcylation suppresses POM121 ubiquitination. Cells overexpressing Myc (tag)-POM121^{WT} or Myc (tag)-POM121^{S199A} were treated with TMG (10 mM, 24 h). Ubiquitinated proteins IP with anti-Myc (tag) antibody and immunoblotted with anti-Ub. Data representative of three experiments. **D** TRIM21 is the E3 ligase for POM121 ubiquitination. Table, Peptides and intensities of POM121 and TRIM21 identified by anti-POM121 IP-MS in H460-BM cells. Bottom, Validation of POM121-TRIM21 interaction by co-IP (cell lysates IP with anti-POM121, blotted with anti-TRIM21). Data representative of three experiments. **E** O-GlcNAcylated POM121 exhibited significantly attenuated binding affinity to TRIM21 in metastatic lineage. H460 and H460-BM cells treated with MG132 (25 nM, 24 h). Cell lysates IP with anti-POM121 and immunoblotted for TRIM21 and ubiquitin. Data representative of three experiments. **F** OGT regulates POM121-TRIM21 binding. Left, H460 cells transfected with EV (empty vector) or 3× Flag-OGT plasmid. Right, H460-BM cells transfected with NC or si-OGT. Co-IP with anti-POM121 and immunoblot for TRIM21. Data representative of three experiments. **G** O-GlcNAcylation of Ser199 disrupts POM121-TRIM21 binding. Left, Cells expressing Myc (tag)-POM121^{WT} or Myc (tag)-POM121^{S199A} treated with TMG (10 mM, 24 h). Right, Cells co-transfected with 3× Flag-OGT plasmid. Co-IP with anti-Myc (tag) and immunoblot for HA-tagged TRIM21. Data representative of three experiments.

dependent POM121 stabilization governs c-MYC nuclear translocation efficiency.

To investigate whether c-MYC nuclear translocation drives NSCLC bone metastasis, we reconstituted c-MYC expression in POM121-knockdown H460-BM cells, which restored nuclear c-MYC accumulation (Fig. 4H) and substantially rescued the bone colonization defect induced by POM121 depletion in nude mouse intracardiac injection models (Fig. 4I, J). These findings establish POM121 as a key bone metastasis regulator through c-MYC nuclear translocation in NSCLC.

c-MYC facilitates bone metastasis via transcriptional activation of ECM-associated genes

To define how POM121-facilitated c-MYC drives bone metastasis, RNA-seq of POM121^{KD} vs. POM121^{WT} cells identified extracellular matrix (ECM)-associated pathways as key c-MYC transcriptional targets functionally linked to bone metastasis (Fig. 5A). RT-qPCR confirmed significant downregulation of these genes in H460-BM$^{POM121\text{-}KD}$ cells (Fig. 5B), while POM121 overexpression in H460 cells upregulated their expression (Fig. S5A). Complementary to this, c-MYC knockdown in H460-BM cells similarly suppressed ECM gene expression (Fig. 5C), and c-MYC overexpression in H460 cells recapitulated this activation (Fig. S5B). These data demonstrate POM121-mediated c-MYC nuclear translocation transcriptionally activates ECM genes. Building on O-GlcNAcylation-dependent POM121 stabilization in metastatic cells, OGT knockdown reduced POM121 O-GlcNAcylation and downregulated ECM genes (Fig. 5D), whereas TMG enhanced O-GlcNAcylation in low-metastatic H460 cells upregulated ECM genes (Fig. S5C). Collectively, elevated OGT in H460-BM cells enhances POM121 O-GlcNAcylation, stabilizes POM121 to promote c-MYC nuclear import, and activates ECM gene transcription, establishing the complete OGT-POM121-c-MYC-ECM axis driving NSCLC bone metastasis.

ECM-associated genes critically drive tumor metastasis by remodeling the tumor microenvironment [30, 31], primarily through PI3K-AKT-mTOR or RAS-RAF-MEK-ERK pathway activation [32]. Western blotting revealed enhanced phospho-activation of PI3K-AKT-mTOR components in bone-metastatic H460-BM compared to H460-BM$^{POM121\text{-}KD}$ cells (Fig. 5E), with POM121 overexpression in H460 cells similarly enhancing pathway activation (Fig. S5D), establishing that c-MYC-driven ECM upregulation activates PI3K-AKT-mTOR cascade. Consistently, c-MYC knockdown in H460-BM suppressed pathway activation (Fig. 5F), while c-MYC overexpression in H460 enhanced it (Fig. S5E). Mechanistically, reducing POM121 O-GlcNAcylation decreased PI3K/AKT/mTOR phosphorylation (Fig. 5G), whereas augmenting O-GlcNAcylation increased PI3K/AKT/mTOR activation (Fig. S5F). Crucially, NSCLC patient data showed positive correlations between ECM gene expression and both POM121/c-MYC levels (Fig. 5H, S5G), confirming clinical relevance of the POM121-c-MYC-ECM axis in driving NSCLC bone metastasis through ECM-mediated PI3K-AKT-mTOR signaling.

Conservation of the OGT-POM121-c-MYC-ECM axis drives bone metastasis in heterogeneous NSCLC models

To validate pan-NSCLC relevance of the O-GlcNAcylated POM121-c-MYC-ECM axis, we generated bone-metastatic subpopulations (H1299-BM, H1437-BM) via iterative in vivo selection after intracardiac injection of H1299/H1437 cells into nude mice. Western blotting revealed markedly elevated OGT and POM121 protein in bone-metastatic subpopulations relative to their parental cell lines (Fig. 6A, S6A). Notably, sWGA pulldown revealed substantially increased O-GlcNAcylation levels of POM121 in bone-metastatic lineages (Fig. 6B, S6B). Furthermore, gain- and loss-of-function experiments confirmed that OGT directly regulates POM121 O-GlcNAcylation (Fig. 6C, S6C). Mechanistically, enhanced O-GlcNAcylation attenuated POM121-TRIM21 binding, reducing ubiquitination and stabilizing POM121 in metastatic variants (Fig. 6D, S6D). Additionally, nucleocytoplasmic fractionation assays demonstrated enhanced POM121-mediated c-MYC nuclear translocation (Fig. 6E, S6E), driving transcriptional activation of ECM genes and PI3K-AKT-mTOR phosphorylation (Fig. 6F, S6F) in metastatic lineages. These collective findings establish the OGT-POM121-c-MYC-ECM axis as a conserved driver of bone metastasis across heterogeneous NSCLC models.

High expression of OGT, POM121, and c-MYC predicts poor prognosis in NSCLC

To validate clinical relevance of the OGT-POM121-c-MYC axis, analysis of NSCLC databases revealed significantly upregulated POM121 in tumors compared to adjacent normal tissues (Fig. 6G). Critically, high co-expression of POM121 and c-MYC robustly correlated with reduced overall survival in these patient cohorts (Fig. 6H). The GSE225208 RNA-seq cohort [33], bulk-seq database of a clinical cohort of LUAD patients, confirmed elevated POM121 and c-MYC expression in bone metastases (Fig. 6I). Furthermore, consistent with their roles as upstream and downstream effectors within the POM121 signaling axis, expression levels of OGT and c-MYC were concomitantly increased in tumor specimens (Fig. S6G). Critically, heightened expression of either OGT or c-MYC similarly predicted adverse clinical outcomes (Fig. S6H). These results collectively validate the OGT-POM121-c-MYC-ECM regulatory axis as both a promising prognostic biomarker and a potential therapeutic target in NSCLC pathogenesis.

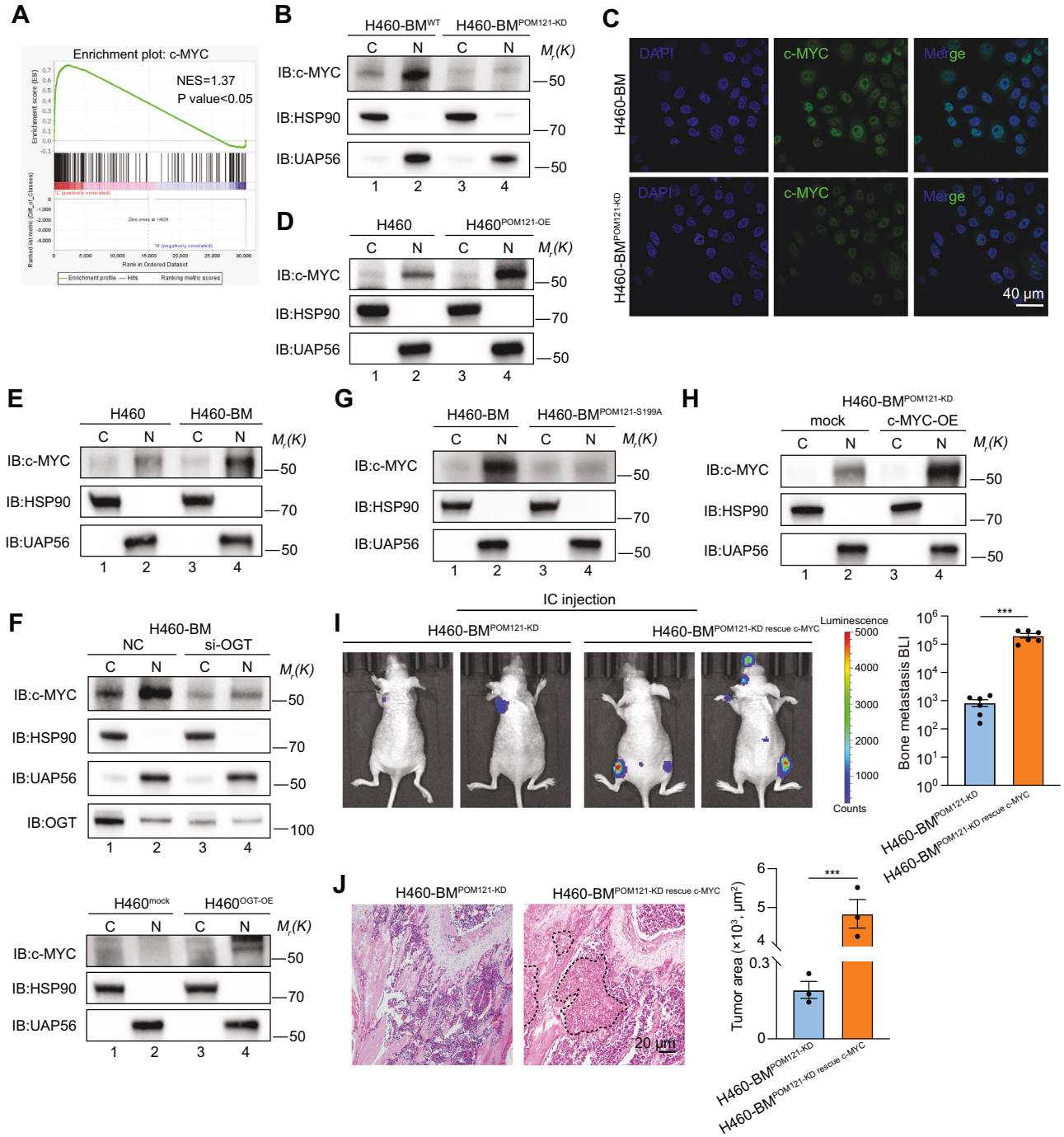

Fig. 4 POM121 promotes c-MYC nuclear translocation to drive bone metastasis. A Enrichment of c-MYC targeting gene signatures in H460-BM cells relative to POM121^{KD} controls. Gene Set Enrichment Analysis (GSEA) of transcriptome meta-analysis data. **B** Immunoblots of c-MYC levels in the nucleoplasm and cytoplasm of H460-BM cells or H460-BM$^{POM121\text{-}KD}$ cells. HSP90 and UAP56 served as fractionation controls. Data representative of three experiments. **C** Immunostaining analysis of c-MYC (green) cellular localization in H460-BM and H460-BM$^{POM121\text{-}KD}$ cells. Scale bar, 40 μm. **D** Immunoblots of c-MYC levels in the nucleoplasm and cytoplasm of H460 cells or H460$^{POM121\text{-}OE}$ cells. HSP90 and UAP56 served as fractionation controls. Data representative of three experiments. **E**, **F** c-MYC subcellular distribution modulated by OGT. **E** H460 and H460-BM cells. **F** Top, H460-BM cells transfected with NC or si-OGT. Bottom, H460 cells transfected with EV or 3× Flag-OGT plasmid. HSP90 and UAP56 served as fractionation controls. Data representative of three experiments. **G** Immunoblots of c-MYC in the nucleoplasm and cytoplasm of H460-BM or H460-BM$^{POM121\text{-}S199A}$ cells. HSP90 and UAP56 served as fractionation controls. Data representative of three experiments. **H** Immunoblots of c-MYC levels in the nucleoplasm and cytoplasm of H460-BM$^{POM121\text{-}KD}$ and H460-BM$^{POM121\text{-}KD\ rescue\ c\text{-}MYC}$ cells. HSP90 and UAP56 served as fractionation controls. Data representative of three experiments. **I**–**J** Rescue of c-MYC protein in the absence of POM121 in NSCLC promotes metastasis in nude mouse model. **I** Bioluminescence imaging of nude mice four weeks after intracardiac injection of H460-BM$^{POM121\text{-}KD}$ and H460-BM$^{POM121\text{-}KD\ rescue\ c\text{-}MYC}$ cells (1×10^5 cells/mouse). Data are represented as mean ± SEM; $n = 6$ mice/group, ***$p < 0.001$, unpaired t-test. **J** Histological validation and tumor area quantifications of bone metastasis. Representative H&E-stained sections from mice in (**I**). Dashed lines demarcate tumor boundaries. Scale bar, 20 μm. Data are represented as mean ± SEM; ***$p < 0.001$, unpaired t-test.

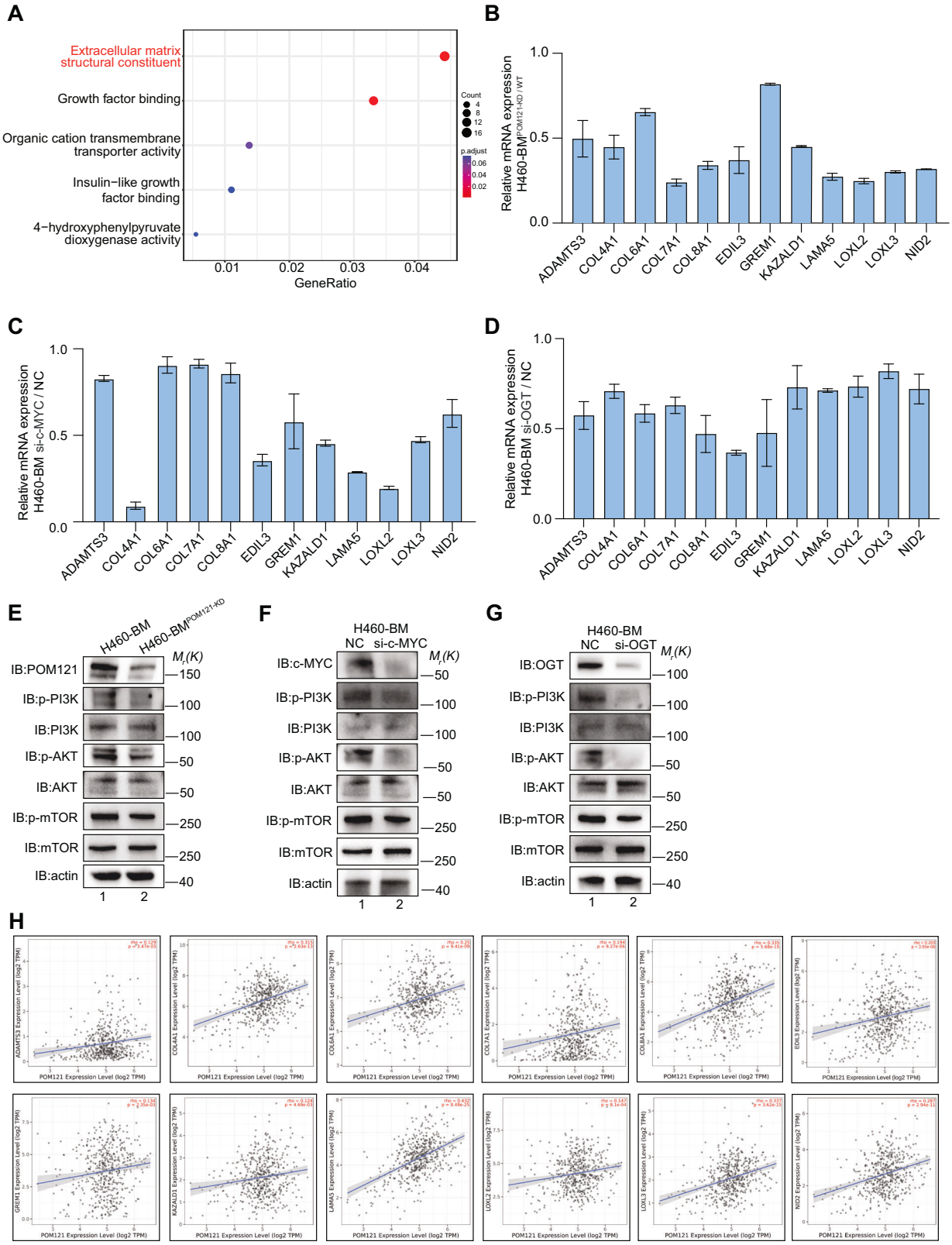

DISCUSSION

The bone metastatic cascade in NSCLC is a complex, multi-step process. Detachment from the primary tumor and intravasation into the circulation represent a critical initial step [7]. During this phase, epithelial-mesenchymal transition (EMT) has been identified as a well-established mechanism enabling NSCLC cells to acquire invasive and metastatic capabilities, and it is tightly regulated by numerous factors [34]. However, the impact of dynamic molecular alterations within tumor cells and the tumor microenvironment (TME), particularly the extracellular matrix

Fig. 5 c-MYC promotes ECM-associated genes transcription and PI3K-AKT-mTOR activation in NSCLC. A Gene Ontology (GO) analysis of biological processes in H460-BM$^{POM121\text{-}KD}$ cells and H460-BM cells. Top 5 significantly enriched pathways from RNA-seq data ($p < 0.05$). **B** Extracellular matrix (ECM)-related genes mRNA levels were analyzed by RT-qPCR between H460-BM and H460-BM$^{POM121\text{-}KD}$ cells. (mean ± SEM; $n = 3$; unpaired t-test). **C** ECM-related genes mRNA levels were analyzed by RT-qPCR between H460-BM and H460-BM$^{c\text{-}MYC\text{-}KD}$ cells. (mean ± SEM; $n = 3$; unpaired t-test). **D** ECM-related genes mRNA levels were analyzed by RT-qPCR between H460-BM and H460-BM$^{OGT\text{-}KD}$ cells. (mean ± SEM; $n = 3$; unpaired t-test). **E** Immunoblot analysis of PI3K-AKT-mTOR pathway activation (p-PI3K/PI3K, p-AKT/AKT, p-mTOR/mTOR) between H460-BM and H460-BM$^{POM121\text{-}KD}$ cells. Data representative of three experiments. **F** Immunoblot analysis of PI3K-AKT-mTOR pathway activation in H460-BM cells transfected with NC or si-c-MYC. Data representative of three experiments. **G** Immunoblot analysis of PI3K-AKT-mTOR pathway activation in H460-BM cells transfected with NC or OGT siRNAs. Data representative of three experiments. **H** Correlation between POM121 and ECM-related genes expression in NSCLC patients (TCGA database). (http://timer.comp-genomics.org). Spearman correlation test rho and p-values are shown.

(ECM), has been comparatively overlooked. To elucidate the molecular mechanisms underlying NSCLC bone metastasis and identify novel diagnostic/therapeutic vulnerabilities, we investigated the molecular landscape distinguishing bone-metastatic (BM) NSCLC cells from their parental counterparts, revealing that O-GlcNAcylation mediated stabilization of POM121 drives bone metastasis in NSCLC.

In this study, we established that POM121 exhibits elevated O-GlcNAcylation levels in bone-metastatic cell lines. This post-translational modification effectively attenuates its interaction with the E3 ubiquitin ligase TRIM21, thereby augmenting POM121 protein stability. Mechanistically, acting as a core NPC component, POM121 facilitates the nuclear translocation of the oncogenic transcription factor c-MYC. This nuclear translocation is pivotal, as c-MYC subsequently orchestrates the transcriptional upregulation of a suite of ECM-related genes. We identify this c-MYC-driven ECM reprogramming as a key downstream effector mechanism directly propagating bone metastatic colonization in our models (e.g., H460, H1299, H1437) (Fig. 7). In addition, we also observed sporadic metastasis to other sites, such as the brain, in our model. These findings may suggest a potential avenue for future research into the broader metastatic propensity regulated by OGT/POM121 signaling.

Importantly, these findings significantly extend beyond POM121. We uncovered a broader cohort of nucleoporins governed by analogous O-GlcNAcylation-mediated stabilization via OGT, which counteracts TRIM21-mediated ubiquitination. This reveals a previously uncharacterized regulatory mechanism for nucleoporins homeostasis during NSCLC progression. Critically, clinical data analysis confirms that elevated expression of NPC components correlates with reduced overall survival in NSCLC patients (Fig. S3E), clinically reinforcing that NPC dysregulation is a critical driver of NSCLC bone metastasis.

While O-GlcNAcylation is well-established as a modulator of cancer progression across diverse malignancies [35–37], its specific interplay with the ubiquitin-proteasome system and impact on nucleoporin stability in metastasis is novel. Intriguingly, we demonstrate that in NSCLC, O-GlcNAcylation antagonizes TRIM21-mediated ubiquitination of NPC components. This mechanism stands in contrast to, yet complements, findings in other cancers. For instance, in pancreatic cancer, hyper-O-GlcNAcylation blocks REGγ-mediated degradation of SIRT7 by disrupting their interaction, thereby stabilizing SIRT7. The accumulated SIRT7 deacetylates histone H3 at lysine 18 (H3K18Ac), leading to transcriptional silencing of tumor suppressor genes to accelerate tumorigenesis [38]. Conversely, in hepatocellular carcinoma (HCC), reduced PCK1 expression promotes CHK2 O-GlcNAcylation at Threonine-378, destabilizing CHK2 and impairing dimer formation, which ultimately enhances CHK2-dependent Rb phosphorylation to drive HCC proliferation [39]. These findings illustrate that O-GlcNAcylation exerts context-dependent roles in distinct cancer types. Specifically, in NSCLC bone-metastatic models, we identified a conserved mechanism whereby O-GlcNAcylation stabilizes nucleoporins (e.g., POM121, NUP153, NUP88). Nevertheless, upstream regulators of OGT upregulation in bone-metastatic cells remain elusive. Future studies will delineate the molecular mechanisms inducing OGT overexpression in NSCLC bone-metastatic models.

c-MYC, a canonical proto-oncogene-encoded transcription factor, extensively regulates proliferation, differentiation, metabolism, and apoptosis [40–43]. While its roles in DNA replication origin firing [44], cell cycle progression [45], metabolic reprogramming (e.g., Warburg effect via LDHA, GLUT1, PKM2) [46], and stemness maintenance [47] are well-documented across cancers. These context-dependent roles enable c-MYC to differentially regulate tumor progression. In NSCLC, we reveal a specific pro-metastatic function that c-MYC promotes bone-metastatic progression by orchestrating ECM-remodeling genes transcription. While this ECM-regulatory role is conserved across NSCLC models (e.g., H460, H1299, H1437), whether c-MYC employs an identical mechanism to promote metastasis in other cancers remains unvalidated and warrants future investigation, potentially revealing tissue-specific metastatic mechanisms.

The tumor microenvironment (TME), comprising tumor cells, non-tumor cells, signaling molecules, particularly the dynamically remodeled ECM, is a critical facilitator of metastatic dissemination and colonization [48–50]. During progression, the ECM undergoes pathological remodeling characterized by excessive collagen cross-linking, disordered elastic fibers, and aberrant proteoglycan deposition, ultimately leading to changes in tissue mechanical properties that serve as key drivers for tumor cell invasion and dissemination [31, 51]. Additionally, cancer cells sense ECM properties through surface receptors, activating downstream signaling networks [52, 53]. Although we establish c-MYC-driven ECM molecule transcription as a core downstream effector promoting bone metastasis in NSCLC, the precise mechanisms by which specific ECM components functionally orchestrate discrete steps within the bone metastatic cascade—from extravasation through to micro-metastatic establishment and overt osteolytic/osteoblastic progression—remain incompletely resolved, necessitating further investigation.

Collectively, our findings delineate a previously unrecognized signaling axis—OGT-mediated O-GlcNAcylation stabilizes nucleoporins including POM121, which facilitates c-MYC nuclear import and consequent ECM reprogramming—that critically promotes bone metastasis in NSCLC. This mechanism not only deepens our understanding of the functional interplay between post-translational modifications and nuclear transport in cancer progression, but also highlights the therapeutic potential of targeting the OGT-NPC-c-MYC-ECM axis.

In the diagnostic realm, this axis may provide a multi-dimensional biomarker portfolio. Clinically, POM121 overexpression correlates strongly with aggressive pathological features—such as lymph node metastasis and advanced tumor stage—positioning it as a robust independent prognostic indicator [54–56]. The assessment of c-MYC overexpression can further refine tumor stratification [57, 58], while measurable serum fragments of degraded ECM components and imaging-based stromal stiffness offer non-invasive indicators of metastatic risk [59–61]. Thus, the POM121-c-MYC-ECM axis may serve as a

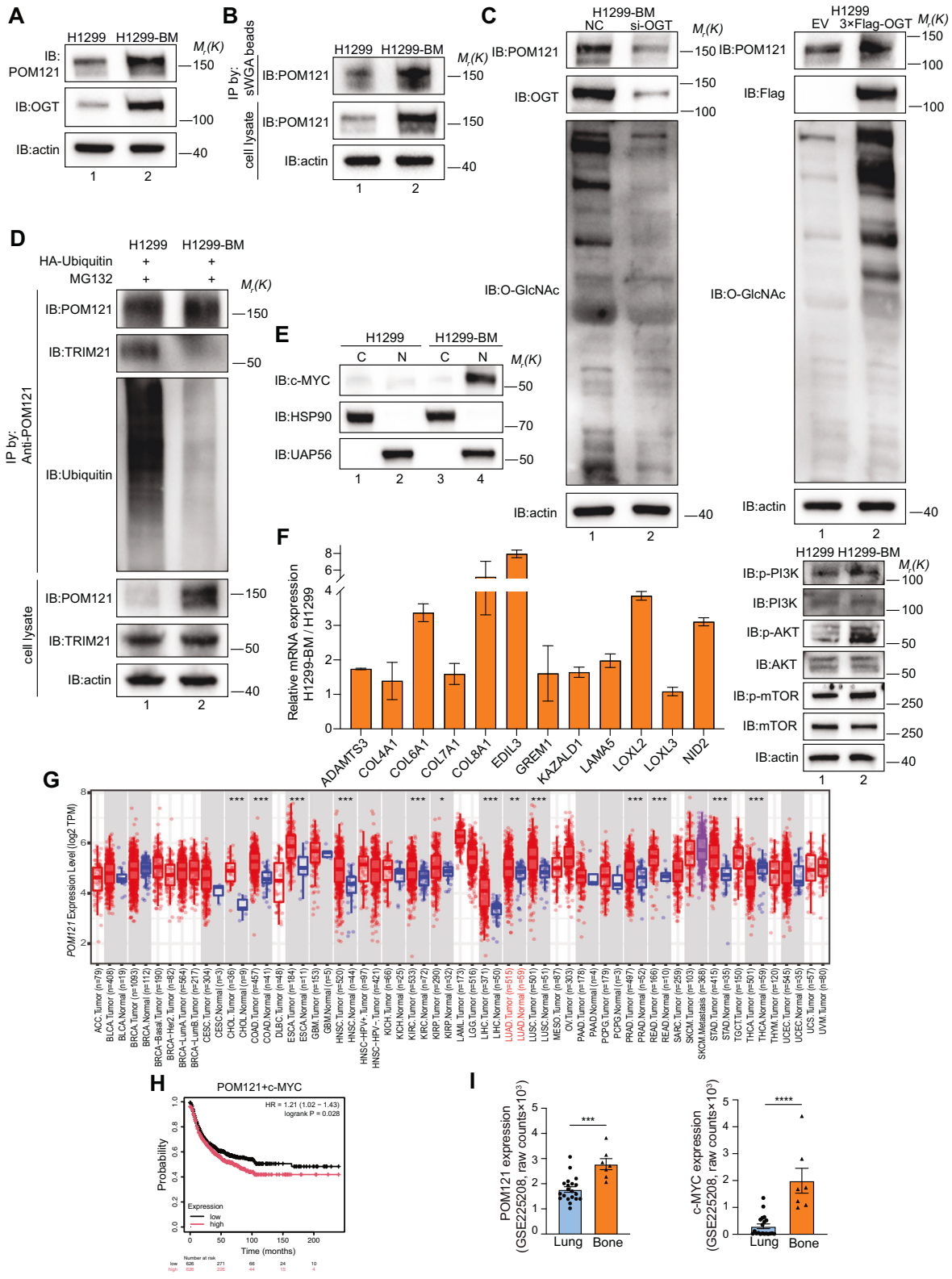

multidimensional biomarker platform for diagnosing and prognosticating bone metastasis in NSCLC.

Therapeutically, our findings pinpoint several actionable nodes. For example, inhibiting ECM-remodeling enzymes, such as lysyl oxidase (LOX) family members, can reduce stromal stiffness and suppress metastasis [62]. In addition, synergistic approaches, like combining antisense oligonucleotides against HIF1A-As2 with c-MYC inhibition, have been shown to attenuate tumorigenesis [63]. It suggests that a combination of inhibitors targeting POM121, c-MYC, and ECM components could simultaneously disrupt multiple steps of this signaling cascade, potentially suppressing bone metastasis in NSCLC. We anticipate that these

Fig. 6 The OGT-POM121-c-MYC-ECM regulatory axis is conserved in H1299 NSCLC cell model. A Analysis of POM121 and OGT expression between parental H1299 and bone-metastatic H1299-BM sublines. Data representative of three experiments. **B**, **C** O-GlcNAcylation stabilizes POM121 in H1299-BM metastatic cells. **B** sWGA pulldown of O-GlcNAcylated proteins from H1299 and H1299-BM lysates, immunoblotted for POM121. **C** Analysis POM121 stability in H1299-BM transfected with OGT siRNAs and H1299 transfected with 3×Flag-OGT plasmid. Data representative of three experiments. **D** O-GlcNAcylated POM121 exhibited significantly attenuated binding affinity to TRIM21 in metastatic lineage. H1299 and H1299-BM cells treated with MG132 (25 nM, 24 h). Cell lysates IP with anti-POM121 and immunoblotted for TRIM21 and ubiquitin. Data representative of three experiments. **E** Enhanced nuclear c-MYC accumulation in metastatic cells. Immunoblots of c-MYC levels in the nucleoplasm and cytoplasm of H1299 cells and H1299-BM cells. HSP90 and UAP56 served as fractionation controls. Data representative of three experiments. **F** Left, ECM-related genes mRNA levels were analyzed by RT-qPCR between H1299 and H1299-BM cells. (mean ± SEM; $n = 3$; unpaired t-test). Right, Analysis of PI3K-AKT-mTOR pathway activation (p-PI3K/PI3K, p-AKT/AKT, p-mTOR/mTOR) between H1299 and H1299-BM cells. Data representative of three experiments. **G** Pan-cancer analysis showed that POM121 was highly expressed in NSCLC. (TCGA data; $^{*}p < 0.05$, $^{**}p < 0.01$, $^{***}p < 0.001$). **H** High POM121 and c-MYC co-expression correlates with poor NSCLC prognosis. Kaplan-Meier overall survival analysis of 2166 NSCLC patients from TCGA, stratified by high/low mRNA expression of POM121 (log-rank test, $p < 0.05$). **I** Significantly elevated POM121 and c-MYC expression in bone metastatic lesions versus primary lung lesions of LUAD patients with bone metastasis. Data derived from the GSE225208 dataset (bulk RNA-seq; $n = 20$ primary lung lesions vs. $n = 7$ bone metastatic lesions, unpaired t-test, $^{***}p < 0.001$, $^{****}p < 0.0001$).

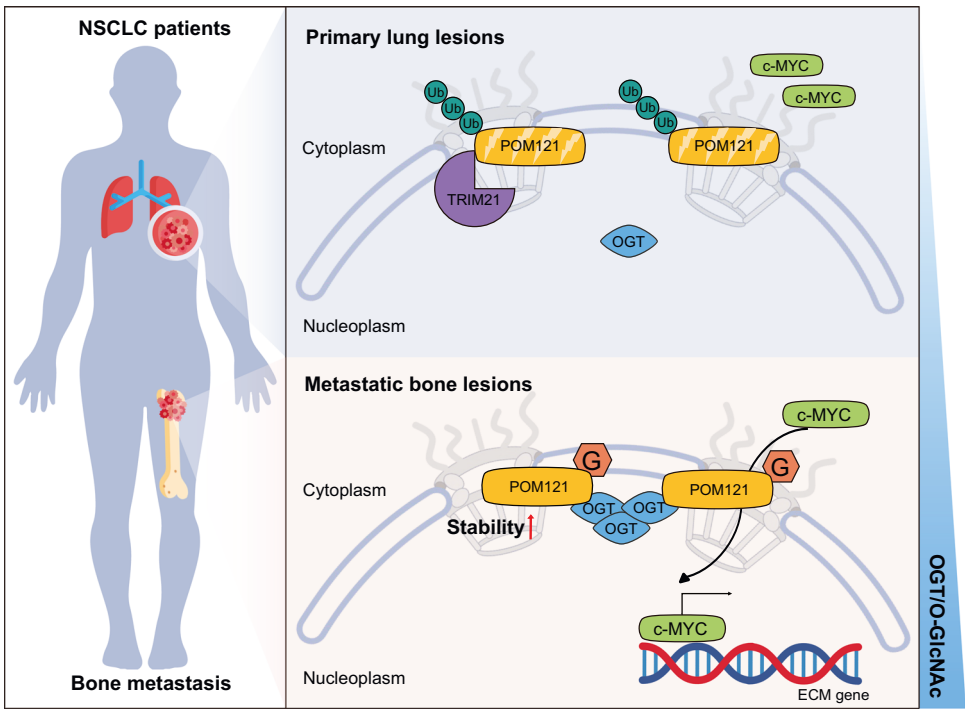

Fig. 7 Schematic of the O-GlcNAcylation-POM121-c-MYC-ECM axis promoting bone metastasis in NSCLC. Elevated O-GlcNAcylation of POM121 in bone-metastatic cells antagonizes ubiquitination by impairing binding to the E3 ubiquitin ligase TRIM21, thereby increasing POM121 protein stability. As a stabilized core NPC component, POM121 facilitates nuclear import of the oncogenic transcription factor c-MYC. Nuclear c-MYC subsequently drives transcription of ECM-related genes, promoting bone metastasis in NSCLC.

insights will open new avenues for early diagnostic strategies and metastasis-directed therapies, ultimately offering hope for mitigating the devastating consequences of bone metastasis in lung cancer patients.

DATA AVAILABILITY

All data presented are available in the main text or the supplementary materials. The raw RNA-seq data have been deposited in the Genome Sequence Archive [64] in National Genomics Data Center [65], China National Center for Bioinformation / Beijing Institute of Genomics, Chinese Academy of Sciences (GSA-Human: HRA014802) that are publicly accessible at https://ngdc.cncb.ac.cn/gsa-human/browse/HRA014802.

REFERENCES

1. Hirsch FR, Scagliotti GV, Mulshine JL, Kwon R, Curran WJ Jr., Wu YL, et al. Lung cancer: current therapies and new targeted treatments. Lancet. 2017;389:299–311.
2. Molina JR, Yang P, Cassivi SD, Schild SE, Adjei AA. Non-small cell lung cancer: epidemiology, risk factors, treatment, and survivorship. Mayo Clin Proc. 2008;83:584–94.
3. Riihimäki M, Hemminki A, Fallah M, Thomsen H, Sundquist K, Sundquist J, et al. Metastatic sites and survival in lung cancer. Lung Cancer. 2014;86:78–84.
4. Wu S, Pan Y, Mao Y, Chen Y, He Y. Current progress and mechanisms of bone metastasis in lung cancer: a narrative review. Transl Lung Cancer Res. 2021;10:439–51.
5. Vicent S, Perurena N, Govindan R, Lecanda F. Bone metastases in lung cancer. Potential novel approaches to therapy. Am J Respir Crit Care Med. 2015;192:799–809.
6. Zhu Y, She J, Sun R, Yan X, Huang X, Wang P, et al. Impact of bone metastasis on prognosis in non-small cell lung cancer patients treated with immune checkpoint inhibitors: a systematic review and meta-analysis. Front Immunol. 2024;15:1493773.
7. Xue M, Ma L, Zhang P, Yang H, Wang Z. New insights into non-small cell lung cancer bone metastasis: mechanisms and therapies. Int J Biol Sci. 2024;20:5747–63.
8. Sone S, Yano S. Molecular pathogenesis and its therapeutic modalities of lung cancer metastasis to bone. Cancer Metastasis Rev. 2007;26:685–9.

9. Pan S, Chen R. Pathological implication of protein post-translational modifications in cancer. Mol Aspects Med. 2022;86:101097.
10. Yang X, Qian K. Protein O-GlcNAcylation: emerging mechanisms and functions. Nat Rev Mol Cell Biol. 2017;18:452–65.
11. Chatham JC, Zhang J, Wende AR. Role of O-Linked N-Acetylglucosamine Protein Modification in Cellular (Patho)Physiology. Physiol Rev. 2021;101:427–93.
12. Cheng SS, Mody AC, Woo CM. Opportunities for Therapeutic Modulation of O-GlcNAc. Chem Rev. 2024;124:12918–3019.
13. Zhao Y, Li R, Wang W, Zhang H, Zhang Q, Jiang J, et al. O-GlcNAc signaling: Implications for stress-induced adaptive response pathway in the tumor microenvironment. Cancer Lett. 2024;598:217101.
14. Liu Y, Yu K, Kong X, Zhang K, Wang L, Zhang N, et al. FOXA1 O-GlcNAcylation-mediated transcriptional switch governs metastasis capacity in breast cancer. Sci Adv. 2023;9:eadg7112.
15. Shi Q, Shen Q, Liu Y, Shi Y, Huang W, Wang X, et al. Increased glucose metabolism in TAMs fuels O-GlcNAcylation of lysosomal Cathepsin B to promote cancer metastasis and chemoresistance. Cancer Cell. 2022;40:1207–22.e10.
16. Beck M, Hurt E. The nuclear pore complex: understanding its function through structural insight. Nat Rev Mol Cell Biol. 2017;18:73–89.
17. Knockenhauer KE, Schwartz TU. The Nuclear Pore Complex as a Flexible and Dynamic Gate. Cell. 2016;164:1162–71.
18. Funakoshi T, Clever M, Watanabe A, Imamoto N. Localization of Pom121 to the inner nuclear membrane is required for an early step of interphase nuclear pore complex assembly. Mol Biol Cell. 2011;22:1058–69.
19. Yavuz S, Santarella-Mellwig R, Koch B, Jaedicke A, Mattaj IW, Antonin W. NLS-mediated NPC functions of the nucleoporin Pom121. FEBS Lett. 2010;584:3292–8.
20. Zhang C, Zhou L, Zhang M, Du Y, Li C, Ren H, et al. H3K18 Lactylation Potentiates Immune Escape of Non-Small Cell Lung Cancer. Cancer Res. 2024;84:3589–601.
21. Kang Y, Siegel PM, Shu W, Drobnjak M, Kakonen SM, Cordón-Cardo C, et al. A multigenic program mediating breast cancer metastasis to bone. Cancer Cell. 2003;3:537–49.
22. Luis-Ravelo D, Antón I, Vicent S, Hernández I, Valencia K, Zandueta C, et al. Tumor-stromal interactions of the bone microenvironment: in vitro findings and potential in vivo relevance in metastatic lung cancer models. Clin Exp Metastasis. 2011;28:779–91.
23. Zhao M-N, Zhang L-F, Sun Z, Qiao L-H, Yang T, Ren Y-Z, et al. A novel microRNA-182/Interleukin-8 regulatory axis controls osteolytic bone metastasis of lung cancer. Cell Death Dis. 2023;14:298.
24. Cox J, Mann M. MaxQuant enables high peptide identification rates, individualized p.p.b.-range mass accuracies and proteome-wide protein quantification. Nat Biotechnol. 2008;26:1367–72.
25. Kim D, Langmead B, Salzberg SL. HISAT: a fast spliced aligner with low memory requirements. Nat Methods. 2015;12:357–60.
26. Subramanian A, Tamayo P, Mootha VK, Mukherjee S, Ebert BL, Gillette MA, et al. Gene set enrichment analysis: a knowledge-based approach for interpreting genome-wide expression profiles. Proc Natl Acad Sci USA. 2005;102:15545–50.
27. Chen L, Hu M, Chen L, Peng Y, Zhang C, Wang X, et al. Targeting O-GlcNAcylation in cancer therapeutic resistance: The sugar Saga continues. Cancer Lett. 2024;588:216742.
28. He X-F, Hu X, Wen G-J, Wang Z, Lin W-J. O-GlcNAcylation in cancer development and immunotherapy. Cancer Lett. 2023;566:216258.
29. Ye L, Ding W, Xiao D, Jia Y, Zhao Z, Ao X, et al. O-GlcNAcylation: cellular physiology and therapeutic target for human diseases. MedComm (2020). 2023;4:e456.
30. Zhang C, Qin C, Dewanjee S, Bhattacharya H, Chakraborty P, Jha NK, et al. Tumor-derived small extracellular vesicles in cancer invasion and metastasis: molecular mechanisms, and clinical significance. Mol Cancer. 2024;23:18.
31. Sleeboom JJF, van Tienderen GS, Schenke-Layland K, van der Laan LJW, Khalil AA, Verstegen MMA. The extracellular matrix as hallmark of cancer and metastasis: From biomechanics to therapeutic targets. Sci Transl Med. 2024;16:eadg3840.
32. Harisi R, Jeney A. Extracellular matrix as target for antitumor therapy. Onco Targets Ther. 2015;8:1387–98.
33. Zhang X, Xiao K, Wen Y, Wu F, Gao G, Chen L, et al. Multi-omics with dynamic network biomarker algorithm prefigures organ-specific metastasis of lung adenocarcinoma. Nat Commun. 2024;15:9855.
34. Huang L, Liu X, Chen Q, Yang J, Zhang D, Zhao Y, et al. TGF-β-induced lncRNA TBUR1 promotes EMT and metastasis in lung adenocarcinoma via hnRNPC-mediated GRB2 mRNA stabilization. Cancer Lett. 2024;600:217153.
35. Zeng X, Chen Z, Zhu Y, Liu L, Zhang Z, Xiao Y, et al. O-GlcNAcylation regulation of RIPK1-dependent apoptosis dictates sensitivity to sunitinib in renal cell carcinoma. Drug Resist Updat. 2024;77:101150.
36. Zhang Y, Sun C, Ma L, Xiao G, Gu Y, Yu W. O-GlcNAcylation promotes malignancy and cisplatin resistance of lung cancer by stabilising NRF2. Clin Transl Med. 2024;14:e70037.
37. Zhu Q, Wang H, Chai S, Xu L, Lin B, Yi W, et al. O-GlcNAcylation promotes tumor immune evasion by inhibiting PD-L1 lysosomal degradation. Proc Natl Acad Sci USA. 2023;120:e2216796120.
38. He X, Li Y, Chen Q, Zheng L, Lou J, Lin C, et al. O-GlcNAcylation and stablization of SIRT7 promote pancreatic cancer progression by blocking the SIRT7-REGγ interaction. Cell Death Differ. 2022;29:1970–81.
39. Xiang J, Chen C, Liu R, Gou D, Chang L, Deng H, et al. Gluconeogenic enzyme PCK1 deficiency promotes CHK2 O-GlcNAcylation and hepatocellular carcinoma growth upon glucose deprivation. J Clin Invest. 2021;131:e144703.
40. Thompson EB. The many roles of c-Myc in apoptosis. Annu Rev Physiol. 1998;60:575–600.
41. Farrell AS, Sears RC. MYC degradation. Cold Spring Harb Perspect Med. 2014; 4.
42. Das SK, Lewis BA, Levens D. MYC: a complex problem. Trends Cell Biol. 2023;33:235–46.
43. Baluapuri A, Wolf E, Eilers M. Target gene-independent functions of MYC oncoproteins. Nat Rev Mol Cell Biol. 2020;21:255–67.
44. Kuzyk A, Mai S. c-MYC-induced genomic instability. Cold Spring Harb Perspect Med. 2014;4:a014373.
45. Bretones G, Delgado MD, León J. Myc and cell cycle control. Biochim Biophys Acta. 2015;1849:506–16.
46. Dang CV. Rethinking the Warburg effect with Myc micromanaging glutamine metabolism. Cancer Res. 2010;70:859–62.
47. Fatma H, Maurya SK, Siddique HR. Epigenetic modifications of c-MYC: Role in cancer cell reprogramming, progression and chemoresistance. Semin Cancer Biol. 2022;83:166–76.
48. Xiao Y, Yu D. Tumor microenvironment as a therapeutic target in cancer. Pharmacol Ther. 2021;221:107753.
49. Jin M-Z, Jin W-L. The updated landscape of tumor microenvironment and drug repurposing. Signal Transduct Target Ther. 2020;5:166.
50. Bader JE, Voss K, Rathmell JC. Targeting Metabolism to Improve the Tumor Microenvironment for Cancer Immunotherapy. Mol Cell. 2020;78:1019–33.
51. Murgai M, Ju W, Eason M, Kline J, Beury DW, Kaczanowska S, et al. KLF4-dependent perivascular cell plasticity mediates pre-metastatic niche formation and metastasis. Nat Med. 2017;23:1176–90.
52. Papanicolaou M, Parker AL, Yam M, Filipe EC, Wu SZ, Chitty JL, et al. Temporal profiling of the breast tumour microenvironment reveals collagen XII as a driver of metastasis. Nat Commun. 2022;13:4587.
53. Gilkes DM, Semenza GL, Wirtz D. Hypoxia and the extracellular matrix: drivers of tumour metastasis. Nat Rev Cancer. 2014;14:430–9.
54. Guan L, Zhang L, Wang T, Jia L, Zhang N, Yan H, et al. POM121 promotes proliferation and metastasis in non-small-cell lung cancer through TGF-β/SMAD and PI3K/AKT pathways. Cancer Biomark. 2021;32:293–302.
55. Wang T, Sun H, Bao Y, En R, Tian Y, Zhao W, et al. POM121 overexpression is related to a poor prognosis in colorectal cancer. Expert Rev Mol Diagn. 2019;20:345–53.
56. Zhou R, Shi C, Tao W, Li J, Wu J, Han Y, et al. Analysis of Mucosal Melanoma Whole-Genome Landscapes Reveals Clinically Relevant Genomic Aberrations. Clin Cancer Res. 2019;25:3548–60.
57. Quigley DA, Dang HX, Zhao SG, Lloyd P, Aggarwal R, Alumkal JJ, et al. Genomic Hallmarks and Structural Variation in Metastatic Prostate Cancer. Cell. 2018;174:758–69.e9.
58. Chatterji S, Krzoska E, Thoroughgood CW, Saganty J, Liu P, Elsberger B, et al. Defining genomic, transcriptomic, proteomic, epigenetic, and phenotypic biomarkers with prognostic capability in male breast cancer: a systematic review. Lancet Oncol. 2023;24:e74–e85.
59. Barney LE, Jansen LE, Polio SR, Galarza S, Lynch ME, Peyton SR. The Predictive Link between Matrix and Metastasis. Curr Opin Chem Eng. 2016;11:85–93.
60. Huang J, Zhang L, Wan D, Zhou L, Zheng S, Lin S, et al. Extracellular matrix and its therapeutic potential for cancer treatment. Signal Transduct Target Ther. 2021;6:153.
61. Li X, Pan J, Liu T, Yin W, Miao Q, Zhao Z, et al. Novel TCF21high pericyte subpopulation promotes colorectal cancer metastasis by remodelling perivascular matrix. Gut. 2022;72:710–21.
62. Miller BW, Morton JP, Pinese M, Saturno G, Jamieson NB, McGhee E, et al. Targeting the LOX/hypoxia axis reverses many of the features that make pancreatic cancer deadly: inhibition of LOX abrogates metastasis and enhances drug efficacy. EMBO Mol Med. 2015;7:1063–76.
63. Yang K, Zhang W, Zhong L, Xiao Y, Sahoo S, Fassan M, et al. Long non-coding RNA HIF1A-As2 and MYC form a double-positive feedback loop to promote cell proliferation and metastasis in KRAS-driven non-small cell lung cancer. Cell Death Differ. 2023;30:1533–49.
64. Zhang S, Chen X, Jin E, Wang A, Chen T, Zhang X, et al. The GSA Family in 2025: A Broadened Sharing Platform for Multi-omics and Multimodal Data. Genomics Proteomics Bioinformatics. 2025;23:qzaf072.

65. Database Resources of the National Genomics Data Center, China National Center for Bioinformation in 2025. Nucleic Acids Res. 2025;53:D30-D44.

ACKNOWLEDGEMENTS

This work was supported by the National Natural Science Foundation of China (82273380, 82472375, 82273418). Select graphical elements in the schemes were adapted from free resources available under the applicable license on Flaticon.com.

AUTHOR CONTRIBUTIONS

Yi-Zhe Ren and Jia-Tao Lou conceived the study; Yi-Zhe Ren, Feng-Lin Du and Lei Wu performed experiments; Yi-Zhe Ren and Ming-Na Zhao designed experiments; Yi-Zhe Ren, Ming-Na Zhao, Lin Wang and Jia-Tao Lou wrote the paper; Lin Wang and Jia-Tao Lou funded the study.

COMPETING INTERESTS

The authors declare no competing interests.

ADDITIONAL INFORMATION

Supplementary information The online version contains supplementary material available at https://doi.org/10.1038/s41388-026-03687-y.

Correspondence and requests for materials should be addressed to Lin Wang or Jia-Tao Lou.